

## ICRF plasma production in gas mixtures in the Uragan-2M stellarator

Yu.V. Kovtun<sup>a,\*</sup>, V.E. Moiseenko<sup>a,b,c</sup>, A.V. Lozin<sup>a</sup>, M.M. Kozulya<sup>a</sup>, R.O. Pavlichenko<sup>a</sup>, N.V. Zamanov<sup>a</sup>, A.N. Shapoval<sup>a</sup>, V.N. Bondarenko<sup>a</sup>, D.I. Baron<sup>a</sup>, S.M. Maznichenko<sup>a</sup>, V.B. Korovin<sup>a</sup>, E.D. Kramskoy<sup>a</sup>, Y.V. Siusko<sup>a</sup>, V.S. Romanov<sup>a</sup>, Yu.P. Martseniuk<sup>a</sup>, A.Yu. Krasiuk<sup>a</sup>, V.M. Listopad<sup>a</sup>, I.E. Garkusha<sup>a,b</sup>, A. Alonso<sup>d</sup>, A. Dinklage<sup>e</sup>, D. Hartmann<sup>e</sup>, Ye. Kazakov<sup>f</sup>, H. Laqua<sup>e</sup>, J. Ongena<sup>f</sup>, T. Stange<sup>e</sup>, T. Wauters<sup>g</sup>, and the Uragan-2M Team

<sup>a</sup> Institute of Plasma Physics of the NSC KIPT, Kharkiv, Ukraine

<sup>b</sup> V.N. Karazin Kharkiv National University, Kharkiv, Ukraine

<sup>c</sup> Ångström Laboratory, Uppsala University, Uppsala, Sweden

<sup>d</sup> Laboratorio Nacional de Fusion, CIEMAT, Madrid, Spain

<sup>e</sup> Max-Planck-Institut für Plasmaphysik, Greifswald, Germany

<sup>f</sup> Laboratory for Plasma Physics, ERM/KMS, Brussels, Belgium

<sup>g</sup> ITER Organization, St. Paul-lez-Durance, France

## ARTICLE INFO

## Keywords:

Plasma production  
Ion cyclotron heating  
Stellarator  
Uragan-2M  
RF power

## ABSTRACT

This paper summarizes previous results and presents new studies on the ICRF plasma creation both in pure gases and gas mixtures. In all the experiments, the two-strap antenna was operated in monopole phasing with applied RF power of  $\sim 100$  kW. The research for plasma creation was carried out at RF frequencies near the fundamental hydrogen cyclotron harmonic.

## 1. Introduction

The European stellarator programme in the EUROfusion consortium focuses on optimized stellarators of the HELIAS (Helical Axis Advanced Stellarator) line, a stellarator optimisation approach based on modular field coils [1]. The optimized superconducting stellarator device Wendelstein 7-X (W7-X) in Greifswald, Germany, is the first HELIAS machine aimed to demonstrate plasmas that extrapolate to power plant requirements can be reached in a stellarator. [2–5]. Three different heating systems are used in W7-X: electron-cyclotron resonance heating (ECRH) [4–7], neutral beam injection (NBI) [6,8] and ion-cyclotron resonance heating (ICRH) becoming available for the forthcoming experimental campaign [6,9]. The radio frequency system in range of ionic cyclotron frequencies (ICRF) is a versatile tool for fast-ion generation, ion heating, wall conditioning and making plasma start-up in W7-X [9–11].

The standard plasma creation and heating method in a magnetic field of 2.5 T for W7-X are ECRH (140 GHz) at the second harmonic (X2-mode and O2-mode, respectively extraordinary (X) and ordinary (O) waves)

[4–7]. In the magnetic field of 1.7 T heating is possible at the 3rd harmonic ECRH frequency (X3-mode) [7,12]. However, calculations have shown that a target plasma ( $T_e \sim 700$  eV,  $N_e \sim 10^{13} \text{ cm}^{-3}$ ) suitable for start-up of the X3-mode is needed [12]. In the X3-mode heating experiment at the Large Helical Device (LHD), target plasma was created with the NBI [13]. On W7-X it is possible to use NBI to create a target plasma for X3-mode. But calculations [14] show that to successfully create NBI plasma in a time of less than  $\sim 0.5$  s, the maximum time during which the NBI beam dump can tolerate the full load [15,16], target plasma is required. Experiments at W7-X showed that NBI with duration up to 0.7 s cannot create plasma [8]. Attempts to start-up at 1.7 Tesla with combined NBI + X3 mode were unsuccessful [8]. So the experimental studies and the theory show that the creation of target plasma remains a problem to solve.

The target plasma for NBI can be created by a non-resonant microwave discharge [17–19]. This approach is used on the Heliotron J [17–19]. It can also be used to produce a target plasma RF discharge for NBI [20]. Such a scenario was used on the Compact Helical System (CHS) [20]. The initial plasma for NBI and X3 ECRH can be created by

\* Corresponding author.

E-mail address: [Ykovtun@kipt.kharkov.ua](mailto:Ykovtun@kipt.kharkov.ua) (Yu.V. Kovtun).

<https://doi.org/10.1016/j.fusengdes.2023.113887>

Received 10 October 2022; Accepted 20 June 2023

Available online 30 June 2023

0920-3796/© 2023 The Author(s). Published by Elsevier B.V. This is an open access article under the CC BY-NC-ND license (<http://creativecommons.org/licenses/by-nc-nd/4.0/>).

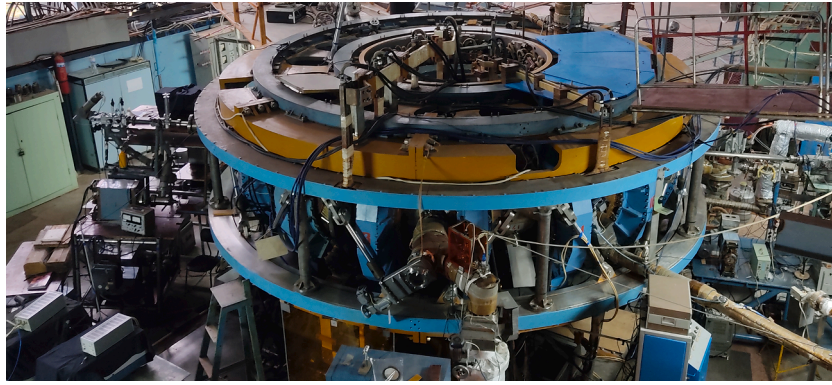


Fig. 1. General view of stellarator Uragan-2 M.

the ICRF system of W7-X [9–11].

A two-strap antenna mimicking the W7-X antenna was installed on stellarator Uragan-2M (U-2M) to make ICRH experiments in support of W7-X [21,22]. The first plasma production ICRF experiments on the U-2M showed the possibility of plasma production with a density up to  $2.6 \times 10^{12} \text{ cm}^{-3}$  in helium at a frequency near the fundamental hydrogen cyclotron harmonic [22]. In these experiments, the optical emission of hydrogen was detected. The small hydrogen minority that spontaneously appeared in the plasma was presumably formed via dissociation of the water vapour and hydro-carbons [21]. Subsequent studies were carried out with controlled hydrogen gas puff [23,24]. The hydrogen minority allowed one to obtain plasma with density more than three times higher as compared with pure helium [23]. In further experiments, plasma production in  $\text{H}_2 + \text{He}$  mixture with an average density of up to  $\sim 10^{13} \text{ cm}^{-3}$  was observed [24]. The minority scenario developed at U-2M [22–24] was also successfully qualified for ICRF plasma generation on the LHD [25]. Earlier RF plasma  $\text{H}_2 + \text{He}$  mixtures in wall conditioning regime were investigated in tokamaks [26–29]. However, the density of plasma obtained in these experiments [26–28] is lower than in the stellarators [23–25].

The studies described below continue the research of ICRF discharge in gas mixtures which was initiated in [22–24]. In addition to the previously used hydrogen and helium gases, deuterium was also used in these studies. Accordingly, it was possible to create both two and three component gas mixtures. Section 2 describes the device, the magnetic system, the vacuum, gas injection, and pressure control systems, the diagnostics and data acquisition systems. Section 3 describes the radio frequency systems, the RF generators and antennas. Section 4 discusses

the experimental results of plasma production at the fundamental ion-cyclotron harmonic of hydrogen. Section 5 summarizes the obtained results.

## 2. Stellarator Uragan-2M

The Uragan-2M device at Kharkiv, Ukraine, is a medium-size stellarator of the torsatron type with major radius  $R = 1.7 \text{ m}$  and minor radius of the vacuum chamber  $r_c = 0.34 \text{ m}$  (see Fig. 1). The U-2M was manufactured and assembled in the early 1990s, was put into operation and briefly exploited, and then conserved [30,31]. It was partially modernized, and put back in operation at the end of 2006 [32–34]. In the following years, the focus of experimental research was on RF plasma production and wall conditioning by RF discharges [35–39]. Since 2017 Institute of Plasma Physics (IPP) of the National Science Center “Kharkov Institute of Physics and Technology” (NSC KIPT) is involved in the EURATOM funded fusion programme EUROfusion (European Consortium for the Development of Fusion Energy) [40]. The stellarator research at IPP KIPT is integrated in the work programme of the EUROfusion Consortium. The research carried out at U-2M supports the experimental program of W7-X. A two-strap antenna mimicking the W7-X antenna is used on U-2M to conduct dedicated ICRF experiments [21,22]. Specific studies focused on RF plasma production scenarios suitable for implementation at W7-X [22–24].

### 2.1. Magnetic system

The U-2M magnetic system is water cooled (see Fig. 2). It includes:

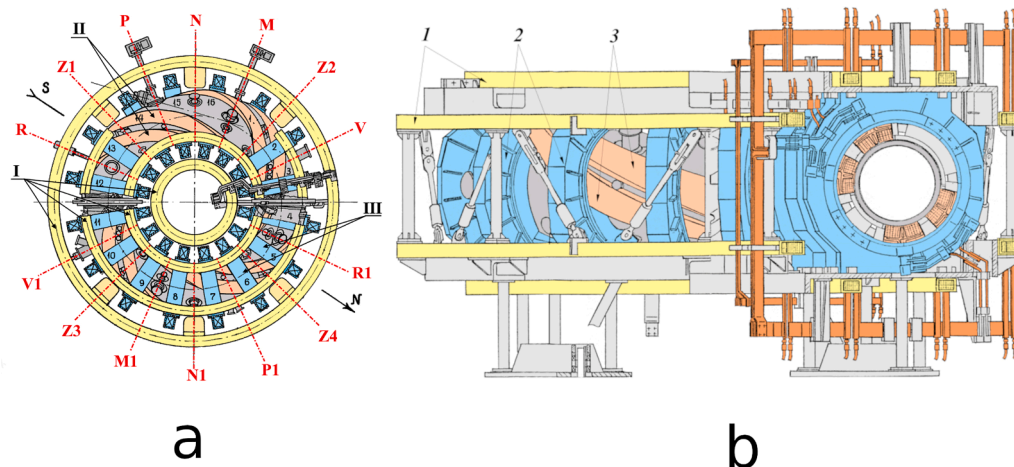


Fig. 2. The schematic view of the U-2M top view (a) and side view (b). Poloidal field (I, 1), toroidal field (III, 2) and helical field coils (II, 3). Different toroidal cross-sections are shown by red lines and denoted by capital letters and numbers.

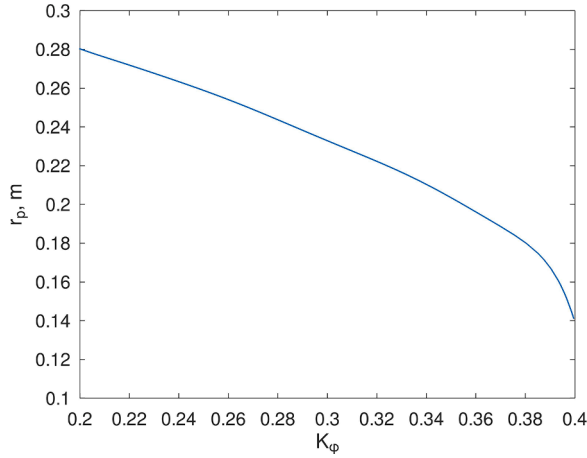


Fig. 3. The average plasma radius versus  $K_\phi$  for U-2M.

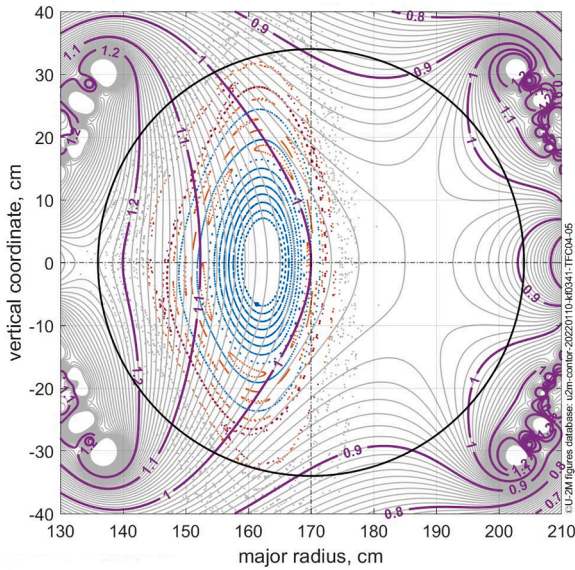


Fig. 4. Poincaré plot of magnetic configuration and contours of magnetic field module at U-2M in cross-sections R1. The circular black line shows the vacuum chamber wall. Gray and purple lines ratio  $B/B_0$ ,  $B_0=0.3274$  T,  $K_\phi=0.3416$ .

helical coil (HC), toroidal coil (TC) and poloidal coil (PC) systems [30, 31, 41, 42]. The HC system consists of two  $l = 2$  helical windings (poles), where each pole is split into two half-poles. The minor radius of the toroidal surface on the helical windings lie is  $r_h = 0.44$  m. The helical winding has four periods ( $m = 4$ ) in the toroidal direction. The TC system consists of is provided by a set of 16 circular toroidal coils evenly distributed along the torus. The PC system that consists of eight coils includes four pairs of compensation windings and two pairs of correction windings. The compensation windings for compensate the vertical field induced by the helical coils. The correction windings control the position and shape of the flux surfaces as well as of the size of the last closed flux surface. With respect to the mechanical stresses, the maximum toroidal magnetic field at the toroidal axis is  $B_0 = 2.4$  T,  $B_0 = B_{tt} + B_{th}$  where  $B_{tt}$  and  $B_{th}$  are the toroidal fields at the geometrical axis of the torus produced by the toroidal and helical coils, respectively [30, 31]. The magnetic configuration parameters can be changed varying the parameter  $K_\phi = B_{th}/(B_{tt} + B_{th})$  and the average vertical magnetic field  $\langle B_z \rangle/B_0$  on the geometric torus axis [42–44]. The PC system that control the magnetic axis position. The average plasma radius  $r_p$  versus  $K_\phi$  is shown in Fig. 3 [30]. For this figure, the configurations the

magnetic field is calculated using the Biot-Savart code, where influence of the current feeds and the detachable joints is taken into account [45]. The calculated magnetic configuration and the magnetic field module distribution at the poloidal cross-section of U-2M shown in fig. 4. At present, two DC source are used to independently power the TC system and the HC system (helical windings and compensation windings are connected in series). Each DC source consists of two flywheel generators P-22-33-17 K with a peak power of 2750 kW each [22]. The generators are operated in a pulsed mode with a pulse duration of a few seconds. The correction windings are powered from a low-power DC generator, which allows smooth tuning of the winding current in the range  $\pm 1$  kA. This magnetic field power system makes it possible to operate at  $B_0 < 0.6$  T.

## 2.2. Vacuum system, gas injection and pressure control

The toroidal vacuum vessel ( $R = 1.7$  m,  $r_c = 0.34$  m) has a volume  $V_c = 3.88$  m<sup>3</sup> (without vacuum ports) and inner surface area of  $S = 22.8$  m<sup>2</sup>. The chamber has 67 ports, which are used for diagnostics, RF heating, working gas injection, vacuum pumping, etc. The ports the vacuum vessel have flanges size: DN40 - 36 pcs., DN100 - 7 pcs., DN120 - 6 pcs., DN160 - 14 pcs., DN200 - 4 pcs. The vacuum vessel is wound with heating tapes for baking. The chamber can be baked up to 100 °C.

The vacuum pumping system of U-2M consists of several pumping units [46]. The AVZ-63D slide-valve mechanical vacuum pump with a pumping speed is up to  $0.063$  m<sup>3</sup> s<sup>-1</sup> for nitrogen/air is used to pump the vacuum vessel up to the fore-vacuum ( $\approx 0.13$  Pa). Three turbo molecular pumps TMN-500 (with liquid nitrogen cryotrap, cross-sections V, Z1 and V1 in Fig. 2a) are used to pump the vacuum vessel U-2M to a high vacuum. The pumping speed of each TMN-500 is up to  $0.5$  m<sup>3</sup> s<sup>-1</sup> for nitrogen/air. The ultimate residual pressure in the vacuum vessel is around  $1 \times 10^{-5}$  Pa.

The gas injection system of the U-2M consists of continuous mass flow system SNA-2-01, additional pulse gas injection system and gas mixture system [47]. The working gases ( $H_2$ ,  $D_2$ , He,  $N_2$ , Ar) or gases mixtures were puffed into the vacuum chamber via a two channels of SNA-2-01 each having pressure stabilization by feedback. The maximal gas flow at atmospheric pressure is not less than  $7 \times 10^{-2}$  (m<sup>3</sup>Pa)/s for nitrogen. For additional pulsed gas injection piezovalve Key High Vacuum Products model PEV-1 is used in the range of gas flow up to 500 SCCM (standard cubic centimetres per minute). The gas mixture system prepares the necessary gas mixture composition for the experiments at U-2M [47]. This system allows to have gas mixture with different pressures inside vacuum chamber with constant percentage of each gas component.

The pressure in the vacuum vessel is measured by several instruments. For the total pressure in the vacuum vessel, the thermocouple gauges PMT-2 operating in the pressure range of 0.13–13 Pa and the ionization gauges PMI-2 in the pressure range of  $2.4 \times 10^{-5}$ –0.13 Pa are used. In plasma experiments, pressure measurements are also performed with cold cathode gauge (Penning gauge) PMM-32-1 and PENNINGVAC transmitter PTR-225S in the pressure range of  $1 \times 10^{-7}$ –1 Pa. To determine the gas composition and partial pressures, a mass spectrometer system is used, which includes the quadrupole mass spectrometer Balzers QMS-420 and the mass-spectrometer IPDO-2 (partial pressure meter omegatron PPMO-2) based on omegatron tube RMO-4S (resonant radio frequency mass spectrometer). The accuracy of gas partial pressure measurements with IPDO-2 without calibration is about 25% and 10% after calibration with a single pure gas.

## 2.3. Diagnostic and data acquisition systems

The spectral diagnostics includes five independent time-resolved optical emission spectroscopy (OES) channels in three cross-sections P1, Z4 and V (see Fig. 2a). Each channel consists of a monochromator-spectrograph (SOLAR TII model MS7501i, MDR-23), a photomultiplier



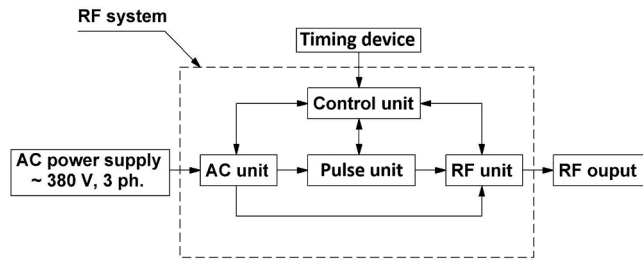


Fig. 5. Circuit diagram of RF systems 'Kaskad'.

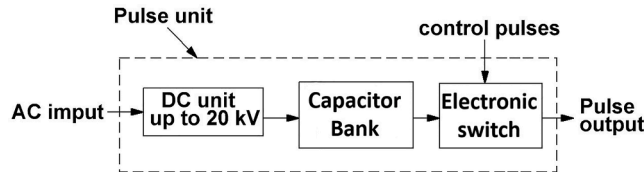


Fig. 6. Circuit diagram of pulse unit.

tube and broadband amplifier. In cross-section P1 it is possible to measure the chord distributions using a shot-by-shot technique [22,24]. The time dependence of the linear electron density averaged over the line of sight was measured using a microwave super-heterodyne interferometer in the cross-section R (see Fig. 2a) [48,49]. For plasma probing a ordinary polarized wave at 140 GHz is used, and the critical electron density is  $2.43 \times 10^{14} \text{ cm}^{-3}$ . The Langmuir probes [23,50], multichord optical diagnostics [50], charge exchange neutral particle analyzers and fast magnetic probe [51] can also be enabled during plasma experiments. Signals from the microwave interferometer and OES system are transmitted via the analog fiber optic links VOLS-1 to a monochromator-spectrograph and then to the data acquisition system (DAS) [52,53]. The DAS of U-2M consists of ADC modules L-CARD E-20-10 (10 MHz, 4 channels), L-783 (3 MHz, 32 channels) and E14-140 (100 kHz, 32 channels) [52,53]. Modules E-20-10 are used to collect data from basic diagnostics such as the microwave interferometer, OES system, gas pressure and other. The currents in the coils of the magnetic system are recorded by module E14-140. The RF directional coupler signal is recorded by the module L-783. The magnetic system, the RF system, the diagnostic equipment and the data acquisition system are all synchronized with the U-2M timing device [54].

### 3. Radio frequency systems

The Uran-2M and Uran-3M (U-3M) stellarators use only RF methods to produce and heat plasma [35–38]. For this purpose, two identical 'Kaskad' pulsed RF systems [55] are used. The 'Kaskad-1' (K-1) and 'Kaskad-2' (K-2) RF systems are designed to operate a wide range of plasma loading resistance, and allow stable power generation during plasma production. The RF systems operate independently of each other. K-1 and K-2 are designed according to the modular principle (see Fig. 5) and have the same circuits, the same design and almost identical characteristics. Each RF system is powered independently of a three-phase AC power supply (see Fig. 5). The AC module transmit the AC power to the other modules. A control module is used to monitor and control the RF system. This module allows both independently and following the signal from the U-2M timing device to start the RF module and the pulse module. This allows the RF system to operate independently from the U-2M. The RF module implements an RF generator circuit.

The pulse unit is used as a pulse power supply for the RF module (see Figs. 5 and 6). It consists of a capacitor bank and a high voltage switch. To charge the capacitors a tuneable high voltage rectifier TDE-5/20 with a maximum output voltage up to 20 kV and a current of up to 5 A is used (see Fig. 6). The capacitor bank with a capacity of  $\approx 1800 \mu\text{F}$  consists of

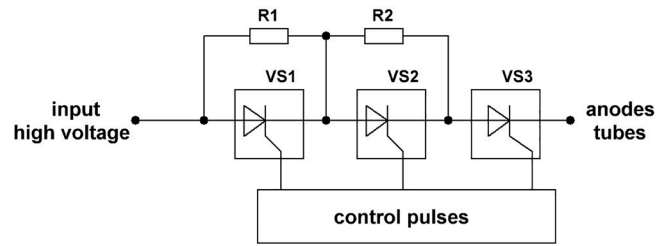


Fig. 7. Circuit diagram of electronic switches.

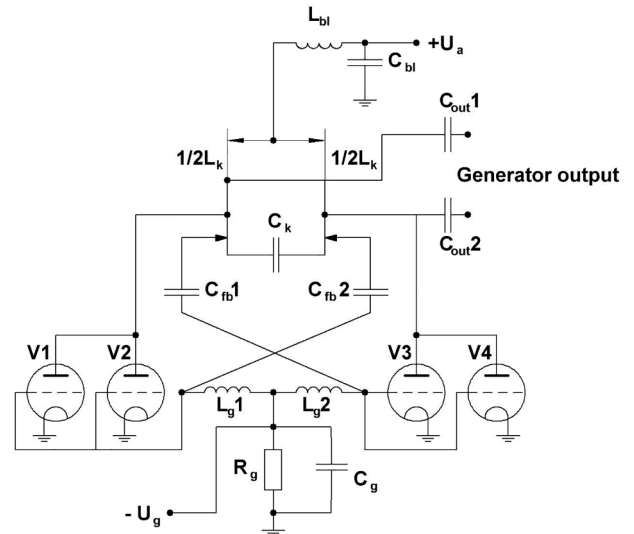


Fig. 8. Circuit diagram of RF generator.

four capacitor sections connected in series with each other. Each section consists of several capacitor assemblies connected in parallel. If one of the capacitor assemblies fails, the others remain operable. Each capacitor assembly contains from 8 to 10 capacitors connected in parallel. Capacitor types IM-5-150 and IM-5-140 with capacity of 150 and 140  $\mu\text{F}$  respectively and maximum voltage up to 5 kV are used in capacitive energy storage.

The voltage from the capacitor bank is fed to the RF module to the anode part of the RF oscillator via the electronic switch (see Figs. 6 and 7). This scheme allows to control the anode voltage during the RF oscillation pulse. The electronic switch consists of three stages, each contains a thyristor assembly VS1, VS2 and VS3 (see Fig. 7). There are 4 thyristors in series on each of VS1 and VS2 and 8 thyristors on VS3. The thyristor assemblies are equipped with thyristors of T3-320 type, which allow switching currents up to 320A in steady state and up to 6.8 kA in short pulse. The electronic switch operates in the following way. When a control pulse is launched by the control unit to the gates of the VS3 thyristor assembly, a reduced anode voltage from a capacitor bank is applied to the RF generator. The voltage value is determined by the capacitor bank voltage reduced by the voltage drop at the resistors R1 and R2. Further, to increase the voltage to the maximum, the thyristor assemblies VS1 and VS2 are switched on, which short-circuit the corresponding resistors. The resistance of the resistors R1 and R2 are chosen so as to provide the desirable mode of formation of the anode voltage pulse. In a typical case, the RF generator anode voltage  $U_a$  is varied stepwise as follows:  $U_{a1} \approx 0.4 \cdot U_a$  at the start,  $U_{a2} \approx 0.6 \cdot U_a$  at step 1 and maximal anode voltage  $U_a$  was set at step 2.

#### 3.1. RF generators

The RF module of the 'Kaskad' pulse RF system (see Fig. 5) is

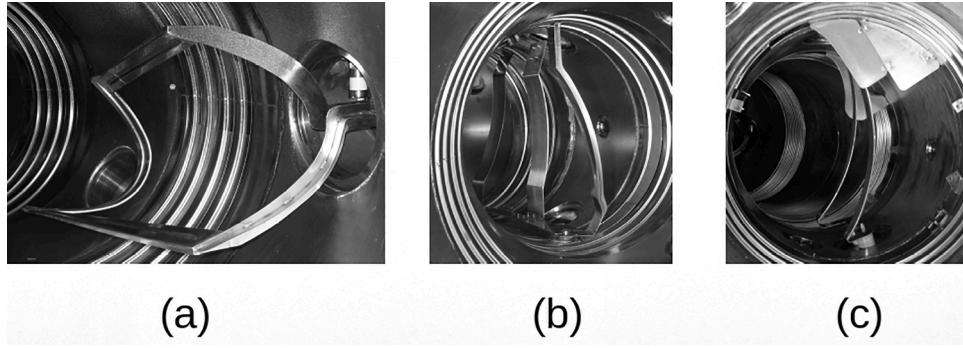


Fig. 9. Photo of the antennas inside the U-2M device, frame antenna (a), three-half-turn antenna (b), two-strap antenna (c).

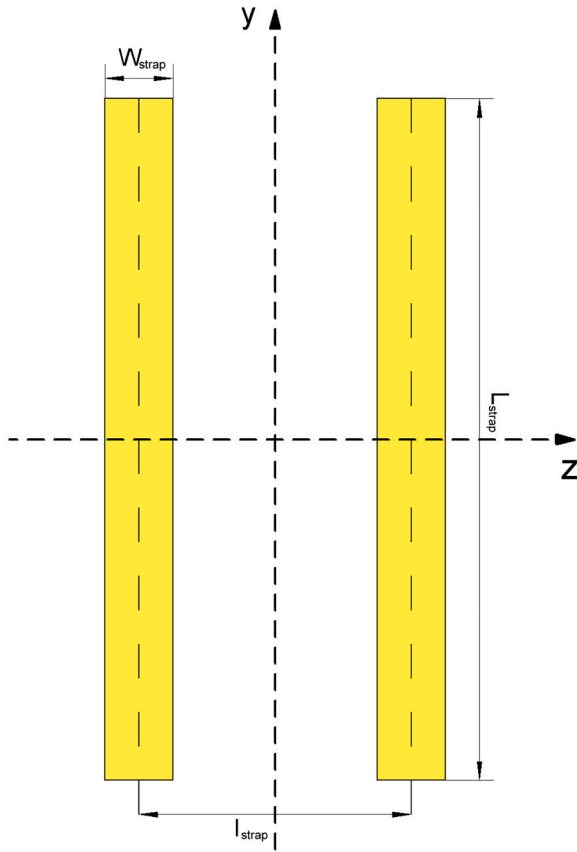


Fig. 10. Sketch of a Two-strap antenna.

implemented with an RF generator circuit. The RF generators have a single-staged push–pull design [55]. Pairs of powerful tubes V1-V4 (see Fig. 8) are connected in parallel at each generator push–pull shoulder with the purpose of doubling the power output without increasing the anode voltage. The GI-26A tubes used in the RF generator are powerful vacuum triodes. They have a liquid cooling. RF module operates at the maximum anode voltage up to 30 kV, generated frequency up to 25 MHz, output RF power up to 3 MW. The frequency of the oscillations generated is changed by replacing the capacitors and varying the inductance of the anode circuit.

The voltage to the anodes of the RF generator tubes is supplied from the pulse module (see Fig. 5). The RF pulse of the oscillator is terminated by applying a locking negative voltage to the grids of the oscillator tubes. The generators operate at a constant frequency in the range of 3–15 MHz. The pulse duration up to 100 ms. The maximum output power of the generators is about 0.8 MW. The power from the RF

generator circuit is launched through the capacitors  $C_{out1}$  and  $C_{out2}$  (see Fig. 8) via the feeder line to the antenna. The output of the generators is balanced. Each of the balanced feeder lines consists of two RK-50-11-13 type RF cables connected in parallel. The aggregate wave impedance of the feeder line is 25  $\Omega$ . At the feeder length  $\approx 26$  m the signal attenuation is  $\approx 0.286$  dB. The amplitude of the forward and reflected waves of the feeder line is measured with directional couplers. The RF power is calculated using the measured amplitudes of the forward and reflected waves.

### 3.2. RF antennas

There are three types of antennas in U-2M: the frame antenna (FA) [36], three-half-turn antenna (THTA) [50] and two-strap antenna (TSA) [21,22]. All antennas can be used to produce plasma. The antennas are located at the outer side of the plasma column at the low field side (see Fig. 9). The FA is located in Z2 cross-section between 1st and 2nd toroidal magnetic coils, the THTA is in N cross-section between 16st and 15nd toroidal magnetic coils, and the TSA is in R1 cross-section (see Fig. 2a).

At the end of 2018, the TSA was installed in the U-2M [21,22]. This antenna is mimicking the W7-X ICRH antenna [9–11] and the main difference is that it is smaller. The antenna consists of two parallel poloidal straps oriented perpendicular to the toroidal axis (see Figs. 9c, 10). Its shape is fitted to the last closed flux surface, and the straps are placed at 10 mm distance from it when the magnetic configuration is with  $K_\phi = 0.32$ . The small limiters are placed at both sides of the antenna (see Fig. 9c). The straps of TSA are made of austenitic stainless steel AISI 321, 2 mm thick. The strap width is  $W_{strap} \approx 0.06$  m, the length is  $L_{strap} \approx 0.6$  m and distance between the middles of the straps  $l_{strap} \approx 0.24$  m. The

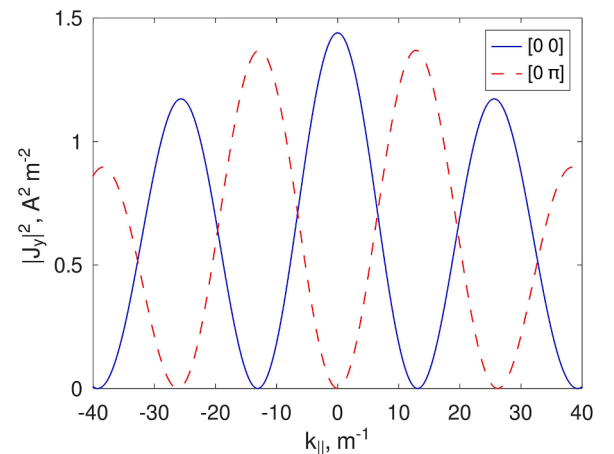


Fig. 11. Spectrum of RF currents excited by two-strap antenna for different toroidal phasings.

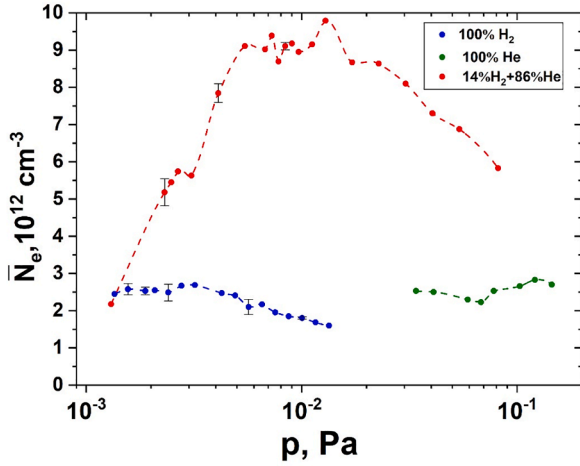


Fig. 12. Maximum average plasma density as a function of the pressure ( $U_a=7$  kV,  $f=4.9$  MHz) 14% $H_2$ +86%He ( $B_0=0.35$  T,  $K_p=0.32$ ), 100% $H_2$  ( $B_0=0.324$  T), 100%He ( $B_0=0.326$  T).

straps and the limiters were coated with a titanium nitride film. In some recent experiments, non-coated straps were also used. More technical details of the TSA are presented in paper [21].

The TSA has four feeding points, and it can have monopole [22] or dipole phasing [21]. To match the impedance of the feeder line to the antenna for monopole phasing, a matching device with a bi-polar L-circuit was used [56]. Using the Fourier transform of the currents on the two straps, the current spectrum of the TSA was calculated [57]:

$$J_y(k_{||}) = J_0 e^{-i\varphi_1} \int_{-W/2-l/2}^{W/2-l/2} e^{-ik_{||}z} dz + J_0 e^{-i\varphi_2} \int_{l/2-W/2}^{W/2+l/2} e^{-ik_{||}z} dz \quad (1)$$

The current density  $J_0$  is assumed to be constant on the strap surface. Neglecting the finite extension and the finite thickness of the strap. A plot of the current spectrum with used phasing monopole phasing [0 0] and dipole phasing [0  $\pi$ ] is shown in Fig. 11.

#### 4. Results and discussion

The gas mixtures were prepared before the experiments in the gas mixture system [47]. The percentage composition of the mixture in the U-2M vacuum chamber was controlled by a mass spectrometer (see Section 2.2). The TSA was used to create the plasma. In the experiments here, the antenna operated in monopole phasing. The antenna was connected to the 'K-1' RF system (see Section 3). The RF frequency was equal to the fundamental hydrogen cyclotron harmonic in these experiments. In this case  $\omega \approx \omega_{ci}(H^+) \approx 2\omega_{ci}(He^{2+}) \approx 2\omega_{ci}(D^+) \approx 4\omega_{ci}(He^+)$ . The cyclotron zone was located inside the plasma column (see, e.g., Fig. 4). In some experiments with the  $D_2+H_2$  mixture, the FA connected to the RF system 'K-2' is used to create a pre-plasma.

##### 4.1. He+H<sub>2</sub> discharge

As in previous experiments, a plasma with a density higher than  $10^{12}$  cm<sup>-3</sup> was created when the RF frequency was close to the fundamental hydrogen cyclotron harmonic [22–24]. The main requirement for this scenario is the presence of minority hydrogen ions in the plasma, for which an ion cyclotron resonance zone exists in the plasma column [22]. The mechanism of plasma formation is ionization by electron impact. Electrons at low plasma densities are heated by a slow wave (SW). At higher densities, the fast wave excited by the antenna is converted to SW at the Alfvén resonance layer. SW propagates toward the lower hybrid resonance layer, where the wave is completely absorbed.

The density of the generated plasma in the He+H<sub>2</sub> mixture depends

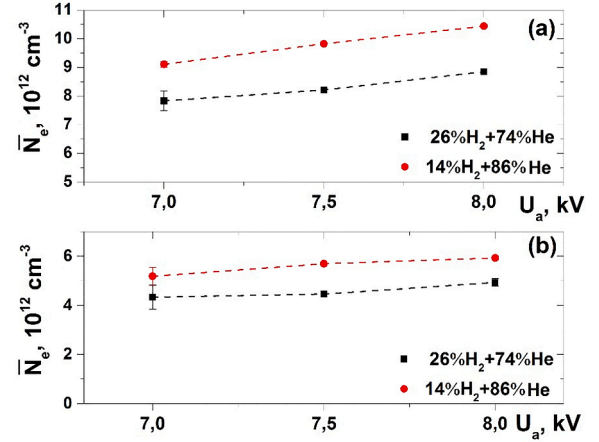
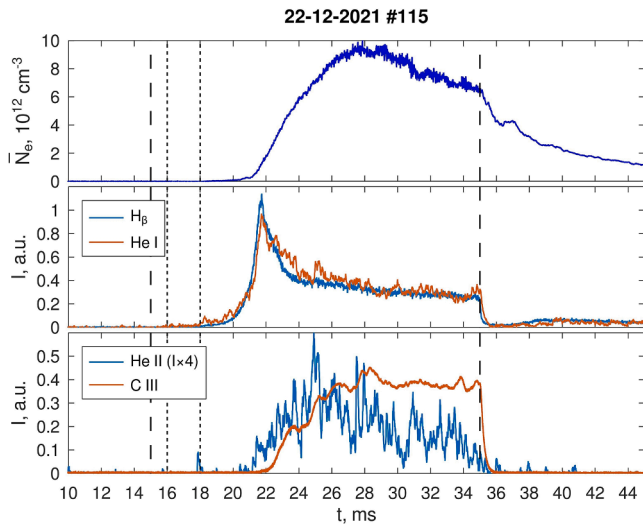


Fig. 13. Maximum average plasma density as a function of the anode voltage on the RF generator. 14% $H_2$ +86%He,  $B_0=0.35$  T,  $f=4.9$  MHz ( $p = 8.4 \times 10^{-3}$  Pa, (a),  $p = 2 \times 10^{-3}$  Pa, (b)) 26% $H_2$ +74%He,  $B_0=0.34$  T,  $f=4.9$  MHz ( $p = 8.2 \times 10^{-3}$  Pa, (a),  $p = 2.3 \times 10^{-3}$  Pa, (b)).

on the hydrogen concentration in the mixture [23,24], the initial pressure of the gas mixture (see Fig. 12) [24], and the injected RF power (see Fig. 13). A plasma with higher density was created at a hydrogen concentration of 14% in the mixture [23,24]. Increasing or decreasing the hydrogen concentration by a factor of  $\approx 2$  leads to some decrease in the plasma density [24]. Such a dependence can be also seen in Fig. 13. Also from Fig. 13 we can see that an increase in the anode voltage on the RF generator 'K-1', which in this case is proportional to the input RF power, leads to an increase in the plasma density. Experiments on the U-2M showed that the RF power density at or above 60 kW/m<sup>3</sup> was necessary to create a high-density plasma. At the same time the temperature of the electrons and plasma ions measured by spectral methods was not more than a few tens of eV.

The average density of plasma formed in the He+H<sub>2</sub> gas mixture was compared with the density of plasma formed in pure helium and hydrogen gases. The injected RF power was almost the same in these experiments at  $\sim 100$  kW. The frequency of the RF generator was near the fundamental frequency of hydrogen cyclotron resonance in hydrogen, and the cyclotron zone was located inside the plasma column. Accordingly, the conditions of plasma creation were similar. The experimental results are shown in Fig. 12. As can be seen, with the same initial pressure of  $\sim 3.5 \times 10^{-2}$  Pa for helium and the He+H<sub>2</sub> mixture, the plasma density is  $\sim 3.2$  times higher in the He+H<sub>2</sub> mixture than in pure helium. Note that an uncontrolled small addition of hydrogen was present in helium which can be concluded from optical measurements. Hydrogen was present in the residual atmosphere of the vacuum chamber. And it could also enter the helium plasma from the wall during the interaction of the plasma wall. When the initial helium pressure decreased below  $\sim 3 \times 10^{-2}$  Pa, the plasma density decreased significantly. In the range of pressures where no dense plasma is formed in helium, for the He+H<sub>2</sub> mixture, a rather dense plasma of  $\approx 8.5 \times 10^{12}$  cm<sup>-3</sup> has been created. The maximum average plasma density obtained in helium did not exceed the value of  $\approx 3 \times 10^{12}$  cm<sup>-3</sup> in the range of pressures below  $\sim 1 \times 10^{-1}$  Pa. Similar results in helium were obtained earlier in [22,23].

The dependence of plasma density on pressure when the hydrogen is pure has general trends with those obtained in helium, but also has significant differences (see Fig. 12). Both in pure hydrogen, as in helium, the maximum average density of plasma is below  $3 \times 10^{12}$  cm<sup>-3</sup>. As the initial pressure increases above  $\sim 2 \times 10^{-2}$  Pa, the plasma density decreases significantly. At an initial pressure of  $\sim 1.5 \times 10^{-2}$  Pa, the plasma density is  $\sim 6.3$  times lower than in the He+H<sub>2</sub> mixture. But as the pressure decreases, this difference in density decreases. At pressures below  $\sim 1.8 \times 10^{-2}$  Pa, the plasma density in hydrogen becomes close to



**Fig. 14.** Time evolutions of average plasma density; optical emission intensities of  $H_{\beta}$ , (486.1 nm), He I (504.7 nm), and ions He II (468.6 nm); C III (464.7 nm), ( $U_a=7.5$  kV,  $f=4.95$  MHz,  $B_0=0.325$  T,  $K_p=0.33$ ,  $I_{corr}=140$  A. Working gas 80% He+10% $H_2$ +10% $D_2$ ,  $p = 9.7 \times 10^{-2}$  Pa). Duty cycle: 15 ms (start), 16 ms (step-1), 18 ms (step-2), 35 ms (shutdown). The vertical lines indicate the times of duty cycle of RF shot.

or slightly higher than that of the He+ $H_2$  mixture.

Note that in both hydrogen and helium, the maximum plasma density changes not strongly, less than  $\sim 2$  times, in the pressure range  $1.5 \times 10^{-3}$  -  $1.5 \times 10^{-2}$  Pa for hydrogen and  $3 \times 10^{-2}$  -  $1.5 \times 10^{-1}$  Pa for helium. In the He+ $H_2$  mixture, the dependence of the maximum average density varies significantly with pressure up to  $\sim 8$  times. Moreover, there is a region of pressures where the maximum density is reached.

The observed difference in the maximum density for pure gases and mixtures cannot be explained only by the difference in the atomic properties of hydrogen and helium. With full ionization and the same number of helium atoms and hydrogen molecules, the maximum density of electrons will be the same. Collision cross sections of electrons with molecule and atom of hydrogen, helium are different. The influence of values of collision cross-sections in He and  $H_2$  on breakdown and plasma creation was analysed in [23]. The analysis showed that the presence of hydrogen in the mixture may lead to better conditions of breakdown and plasma creation. Perhaps the degree of ionization in the mixture can also be achieved higher. The experiments show that the degree of ionization in the mixture is higher (see Fig. 12). This is especially visible in the low pressure region. Increasing the degree of ionization requires energy inputs. Increasing the concentration of electrons in the plasma can also be due to the impurities in plasma. The presence of impurities such as carbon and oxygen was observed by OES in experiments both in pure gases and mixtures [22–24]. However, the increase of the spectral lines of impurities not proportional to density in He+ $H_2$  mixture plasma compared with He and  $H_2$  plasma was not observed.

All this does not fully explain the observed differences in the maximum density for pure gases and the mixture. This difference may be due to the fact that in the plasma of the He+ $H_2$  mixture there is an effective mechanism of energy transfer from the RF wave to the plasma electrons. These mechanisms were discussed above and earlier in [22]. As a result, this leads to a significant increase in the plasma density and degree of ionization. Radiation losses apparently increase, as well as in the LHD experiments [25], and the injected RF power is not sufficient for further heating of the plasma.

ICRF plasma production experiments with  $H_2$ +He mixture can be summarized as follows: (i) gas breakdown and plasma creation are achieved at lower pressure compared to pure He with similar RF power; (ii) plasma density obtained in the mixture is higher than in pure

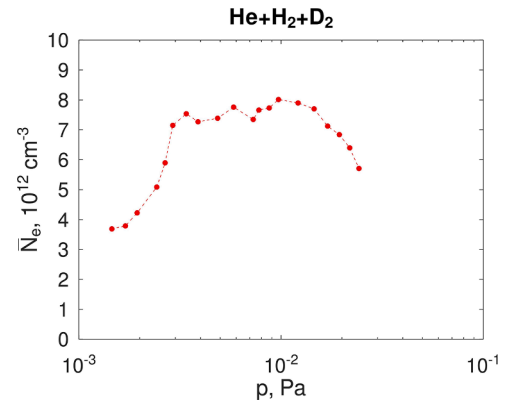


**Fig. 15.** Maximum average plasma density as a function of the pressure. Working gas 80%He+10% $H_2$ +10% $D_2$  ( $U_a=7$  kV,  $f=4.95$  MHz,  $B_0=0.323$  T,  $K_p=0.32$ ,  $I_{corr}=157$  A).

hydrogen (iii) highest plasma densities can be obtained in plasmas with a gas fuelling mixture of 14% hydrogen in helium; (iv) created plasmas have relatively high density ( $10^{13}$  cm $^{-3}$ ) and low ion and electron temperature.

#### 4.2. He+ $H_2$ + $D_2$ discharge

In the He+ $H_2$ + $D_2$  three component gas mixture a similar picture as in the He+ $H_2$  double component gas mixture is observed, namely, the maximum density was observed when the RF frequency was close to the fundamental hydrogen cyclotron harmonic. The time evolutions of the ICRF discharge in the He+ $H_2$ + $D_2$  are presented in Fig. 14. In general, it is similar to the ICRF discharge in the He+ $H_2$  [23,24] with minor differences in the plasma parameters. In the discharge, several stages can be identified. The first stage is the breakdown and production of a plasma with a density below  $10^{12}$  cm $^{-3}$ , which is characterized by the beginning of an increase in the intensity of the spectral lines of the H I and He I atoms (see Fig. 14). At the second stage the plasma density increases to its maximum value. The intensity of the spectral lines of He II and C III ions begins to increase with a short time delay of  $\sim 1$  ms relatively to helium ions (see Fig. 14). This may be due to that helium mainly resides in the volume of the vacuum chamber, while carbon is more on the walls. The intensity of the H I and He I lines increases in the beginning and decreases after  $\sim 22$  ms. A maximum density of  $\approx 9 \times 10^{12}$  cm $^{-3}$  is obtained at  $\sim 28$  ms. Thereafter, the density decreases to  $\approx 6 \times 10^{12}$  cm $^{-3}$ . The intensity of the spectral lines H I, He I and C III practically does not change, the intensity of the helium ion He II decreases. After switching off the RF pulse for at 35 ms, the plasma begins to fade. The intensity of the spectral lines decreases fast. At the stage of decay, after  $\sim 38$  ms, there is an increase in the intensity of the lines H I and He I associated with recombination.

The dependence of the maximum density in the He+ $H_2$ + $D_2$  mixture (see Fig. 15) is similar for the He+ $H_2$  (compare Fig. 12 and [24]). There is a range of optimal pressures where plasma of maximum density is produced. Moreover, this pressure range is somewhat larger for the He+ $H_2$ + $D_2$  than for the He+ $H_2$ . For example, for He+ $H_2$ + $D_2$  the maximum density is observed in the range  $\sim 3 \times 10^{-3}$  -  $1.5 \times 10^{-2}$  Pa (see Fig. 15) for the 14% $H_2$ +86%He mixture the pressure range is  $\sim 5.5 \times 10^{-3}$  -  $1.5 \times 10^{-2}$  Pa. Decreasing the pressure as well as increasing it results in decreasing the plasma density. The obtained plasma density values of  $\approx (7-8) \times 10^{12}$  cm $^{-3}$  in 80.5%He+9% $H_2$ +10.5% $D_2$  are similar to the plasma density values in of 7% $H_2$ +93%He obtained earlier in [24].

Thus, the investigation shows that the ICRF plasma production scenario developed for the He+ $H_2$  mixture [22–24] can be used in the He+ $H_2$ + $D_2$  mixture. The plasma parameters obtained in He+ $H_2$ + $D_2$  do not differ significantly from the plasma parameters in He+ $H_2$ . Note that



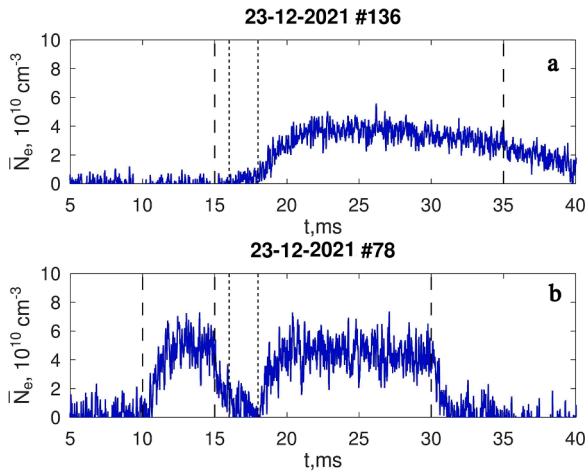


**Fig. 16.** Time evolutions of average plasma density in 14% $H_2$ +86%D $_2$  without pre-ionization #136 (a) ( $U_a = 6$  kV,  $f = 4.95$  MHz,  $B_0 = 0.327$  T,  $K_\phi = 0.325$ ,  $I_{corr} = 133$  A,  $p = 1.4 \times 10^{-2}$  Pa). Duty cycle of TSA: 15 ms (start), 16 ms (step-1), 18 ms (step-2), 35 ms (shutdown). With pre-ionization #78 (b) ( $B_0 = 0.33$  T,  $K_\phi = 0.325$ ,  $I_{corr} = 130$  A,  $p = 2.8 \times 10^{-1}$  Pa). Duty cycle of FA ( $U_a = 5$  kV,  $f = 4$  MHz): 10 ms (start), 15 ms (shutdown). Duty cycle of TSA ( $U_a = 6$  kV,  $f = 5$  MHz): 15 ms (start), 16 ms (step-1), 18 ms (step-2), 30 ms (shutdown). The vertical lines indicate the times of duty cycle of RF shot.

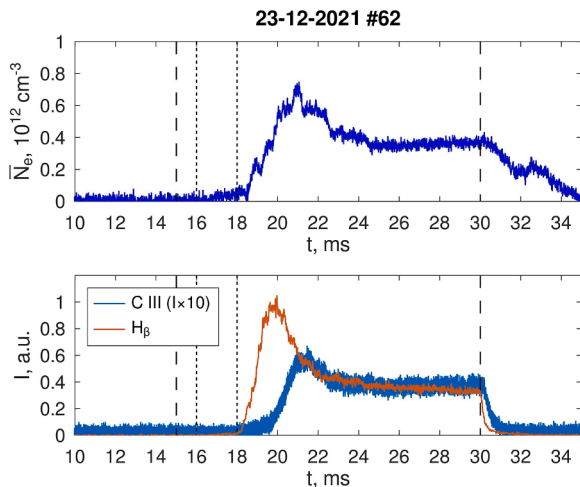


**Fig. 17.** Time evolutions of average plasma density and in 14% $H_2$ +86%D $_2$  optical emission intensities  $H_\beta$ , (486.1 nm), C III (464.7 nm) ( $U_a = 6$  kV,  $f = 4.9$  MHz,  $B_0 = 0.055$  T,  $K_\phi = 0.33$ ,  $p = 1.9 \times 10^{-2}$  Pa. Duty cycle of TSA: 15 ms (start), 16 ms (step-1), 18 ms (step-2), 30 ms (shutdown)). The vertical lines indicate the times of duty cycle of RF shot.

previously the  $^3\text{He}$ -H-D mixture was investigated in ICRH plasma heating experiments [58].

#### 4.3. $D_2+H_2$ discharge

In the case of the  $H_2+D_2$  mixture, the same plasma production scenario was used as for  $He+H_2$ . The results obtained in  $H_2+D_2$  differ significantly from those obtained in the  $He+H_2$  mixture,  $He+H_2+D_2$ , and pure  $He$ ,  $H_2$  gases (see Sections 4.1 and 4.2). As can be seen from Fig. 16a after the RF breakdown and a plasma with a density below  $5 \times 10^{10} \text{ cm}^{-3}$  was created. Changing the initial pressure, the voltage at the antenna  $U_a$ , the generator frequency and the magnetic field value practically did not lead to any significant changes. The introduction of pre-ionization, as seen in Fig. 16b, also did not lead to significant changes.

The collision cross sections of electrons with hydrogen and deuterium are almost the same [59]. Accordingly, the influence of the values of the collision cross sections in  $H_2$  and  $D_2$  on the breakdown and creation of plasma will be minimal. Increasing the hydrogen concentration to more than  $\sim 50\%$  in the mixture significantly increased the density of the created plasma. The achievable plasma density in this case was the same as in pure hydrogen. Reducing the magnitude of the magnetic field when the RF frequency was significantly greater than the ion cyclotron frequency  $\omega \gg \omega_{ci}$ , led to the possibility of creating plasma with a density up to  $7 \times 10^{11} \text{ cm}^{-3}$  (see Fig. 17). And the density was close to that of plasma previously obtained in  $H_2$  [60]. In the case of  $\omega \gg \omega_{ci}$ , the wave propagation conditions are significantly different from the case of  $\omega \approx \omega_{ci}$  and were previously considered in [61]. Thus, changes in the conditions of wave propagation in plasma show that in low magnetic fields when  $\omega \gg \omega_{ci}$  the situation with the formation of plasma in the  $H_2+D_2$  mixture practically does not differ from the creation of plasma in  $H_2$ . But significantly differs in the case of  $\omega \approx \omega_{ci}$ . Thus, additional studies are required for the ICRF scenario of plasma creation in the  $H_2+D_2$  mixture.

## 5. Summary

The ICRF plasma production experiments with  $H_2+He$  mixture showed that the gas breakdown and plasma creation are achieved at lower pressure compared to operation with pure  $He$  and similar RF power. Adding a hydrogen minority allowed one to triple the plasma density as compared with pure helium. The highest plasma density ( $10^{13} \text{ cm}^{-3}$ ) was obtained at a gas fuelling mixture of 14% hydrogen in helium. While addition of deuterium minority to the  $H_2+He$  mixture leads to small changes in the parameters and characteristics of the plasma, in the  $D_2+H_2$  mixture and a low hydrogen concentration (15–20%), only a low  $\sim$  density plasma of no more than  $10^{11} \text{ cm}^{-3}$  is produced. At very low magnetic fields plasma is successfully produced in deuterium.

## Declaration of Competing Interest

The authors declare that they have no known competing financial interests or personal relationships that could have appeared to influence the work reported in this paper.

## Data availability

Data will be made available on request.

## Acknowledgments

This work has been carried out within the framework of the EUROfusion Consortium, funded by the European Union via the Euratom Research and Training Programme (Grant Agreement No 101052200 — EUROfusion). Views and opinions expressed are however those of the author(s) only and do not necessarily reflect those of the European Union or the European Commission. Neither the European Union nor the European Commission can be held responsible for them.

## References

- [1] European Research Roadmap to the Realisation of Fusion Energy, Programme Manager, EUROfusion, Garching/Munich, Germany, 2018.
- [2] G. Grieger, et al., Physics optimization of stellarators, Phys. Fluids B 4 (1992) 2081–2091, <https://doi.org/10.1063/1.860481>.
- [3] F. Warmer, et al., From W7-X to a HELIAS fusion power plant: motivation and options for an intermediate-step burning-plasma stellarator, Plasma Phys. Control. Fusion 58 (2016), 074006, <https://doi.org/10.1088/0741-3335/58/7/074006>.
- [4] T. Klinger, et al., Overview of first Wendelstein 7-X high-performance operation, Nucl. Fusion 59 (2019), 112004, <https://doi.org/10.1088/1741-4326/ab03a7>.



- [5] R.C. Wolf, et al., Performance of Wendelstein 7-X stellarator plasmas during the first divertor operation phase, *Phys. Plasmas* 26 (2019), 082504, <https://doi.org/10.1063/1.5098761>.
- [6] M. Endler, et al., Wendelstein 7-X on the path to long-pulse high-performance operation, *Fusion Eng. Des.* 167 (2021), 112381, <https://doi.org/10.1016/j.fusengdes.2021.112381>.
- [7] V. Erckmann, et al., Electron cyclotron heating for W7-X: physics and technology, *Fusion Sci. Technol.* 52 (2007) 291–312, <https://doi.org/10.13182/FST07-A1508>.
- [8] S.A. Lazerson, et al., First neutral beam experiments on Wendelstein 7-X, *Nucl. Fusion*. 61 (2021), 096008, <https://doi.org/10.1088/1741-4326/ac121c>.
- [9] D.A. Castaño Bardawil, et al., Design improvements, assembly and testing of the ICRH antenna for W7-X, *Fusion Eng. Des.* 166 (2021), 112205, <https://doi.org/10.1016/j.fusengdes.2020.112205>.
- [10] J. Ongena, et al., Study and design of the ion cyclotron resonance heating system for the stellarator Wendelstein 7-X, *Phys. Plasmas* 21 (2014), 061514, <https://doi.org/10.1063/1.4884377>.
- [11] J. Ongena, et al., The ICRH system for the stellarator Wendelstein 7-X, *AIP Conf. Proc.* 2254 (2020), 070003, <https://doi.org/10.1063/5.0014264>.
- [12] N.B. Marushchenko, et al., Reduced field Scenario with X3 heating in W7-X, *EPJ Web Conf.* 203 (2019) 01006, <https://doi.org/10.1051/epjconf/201920301006>.
- [13] T. Shimozuma, et al., Optimization of the high harmonic ECRH scenario to extend a heating plasma parameter range in LH2, *Nucl. Fusion* 55 (2015), 063035, <https://doi.org/10.1088/0029-5515/55/6/063035>.
- [14] D. Gradic, et al., Assessment of the plasma start-up in Wendelstein 7-X with neutral beam injection, *Nucl. Fusion* 55 (2015), 033002, <https://doi.org/10.1088/0029-5515/55/3/033002>.
- [15] S. Äkäsloppolo, et al., Validating fast-ion wall-load IR analysis-methods against W7-X NBI empty-torus experiment, *J. Instrum.* 14 (2019) P07018, <https://doi.org/10.1088/1748-0221/14/07/P07018>.
- [16] P. van Eeten, et al., W7-X NBI beam dump thermocouple measurements as safety interlock, *Fusion Eng. Des.* 146 (2019) 1329–1333, <https://doi.org/10.1016/j.fusengdes.2019.02.069>.
- [17] S. Kobayashi, et al., Plasma startup using neutral beam injection assisted by 2.45 GHz microwaves in Heliotron J, *Nucl. Fusion* 51 (2011), 062002, <https://doi.org/10.1088/0029-5515/51/6/062002>.
- [18] S. Kobayashi, et al., Study of seed plasma generation for NBI plasma start-up using non-resonant microwave launch in Heliotron J, *Plasma Phys. Control. Fusion* 62 (2020), 065009, <https://doi.org/10.1088/1361-6587/ab877e>.
- [19] S. Kobayashi, et al., Role of pre-ionization in NBI plasma start-up of Heliotron J using non-resonant microwave heating, *Nucl. Fusion* 61 (2021), 116009, <https://doi.org/10.1088/1741-4326/ac2105>.
- [20] O. Kaneko, et al., Confinement characteristics of high power heated plasma in CHS, in: *Plasma Physics and Controlled Nuclear Fusion Research 1990, 13th Conference Proceedings Vol. 2*, 1990, pp. 473–481.
- [21] A.V. Lozin, et al., Two-strap RF antenna in URAGAN-2M stellarator, *Probl. At. Sci. Technol. Ser.: Plasma Phys.* 6 (2020) 10–14, <https://doi.org/10.46813/2020-130-010>.
- [22] V. Moiseenko, et al., First experiments on ICRF discharge generation by a W7-X-like antenna in the Uragan-2M stellarator, *J. Plasma Phys.* 86 (2020), 905860517, <https://doi.org/10.1017/S0022377820001099>.
- [23] V. Moiseenko, et al., Plasma production in ICRF in the Uragan-2M stellarator in hydrogen–helium gas mixture, *J. Fusion Energy* 41 (2022) 15, <https://doi.org/10.1007/s10894-022-00326-8>.
- [24] Yu.V. Kovtun, et al., ICRF plasma production with the W7-X Like antenna in the Uragan-2M stellarator, *Plasma Fusion Res.* 17 (2022), 2402034, <https://doi.org/10.1585/pfr.17.2402034>.
- [25] S. Kamio, et al., First experiments on plasma production using field-aligned ICRF fast wave antennas in the large helical device, *Nucl. Fusion* 61 (2021), 114004, <https://doi.org/10.1088/1741-4326/ac277b>.
- [26] A. Lysoivan, et al., Development of ICRF wall conditioning technique on divertor-type tokamaks ASDEX Upgrade and JET, *J. Nucl. Mater.* 337–339 (2005) 456–460, <https://doi.org/10.1016/j.jnucmat.2004.07.060>.
- [27] A. Lysoivan, et al., New scenarios of ICRF wall conditioning in TEXTOR and ASDEX Upgrade, *J. Nucl. Mater.* 363–365 (2007) 1358–1363, <https://doi.org/10.1016/j.jnucmat.2007.01.186>.
- [28] A. Lysoivan, et al., Influence of toroidal and vertical magnetic fields on Ion Cyclotron Wall Conditioning in tokamaks, *J. Nucl. Mater.* 390–391 (2009) 907–910, <https://doi.org/10.1016/j.jnucmat.2009.01.233>.
- [29] G. Sergienko, et al., Ion cyclotron wall conditioning in reactive gases on TEXTOR, *J. Nucl. Mater.* 390–391 (2009) 979–982, <https://doi.org/10.1016/j.jnucmat.2009.01.252>.
- [30] V.E. Bykov, et al., URAGAN-2M: a torsatron with an additional toroidal field, *Fusion Technol.* 17 (1990) 140–147, <https://doi.org/10.13182/FST90-A29177>.
- [31] O.S. Pavlichenko, First results from the 'URAGAN-2M' torsatron, *Plasma Phys. Control. Fusion*. 35 (1993) B223–B230, <https://doi.org/10.1088/0741-3335/35/SB/018>.
- [32] V.I. Tereshin, et al., Researches on plasma physics and controlled fusion in IPP NSC KIPT, *Probl. At. Sci. Technol. Ser.: Plasma Phys.* 6 (2006) 3–9.
- [33] V.E. Moiseenko, et al., RF plasma production in Uragan-2M torsatron, *AIP Conf. Proc.* 933 (2007) 115–118, <https://doi.org/10.1063/1.2800455>.
- [34] A.A. Beletskii, et al., First results of the renewed URAGAN-2M torsatron, *Probl. At. Sci. Technol. Ser.: Plasma Phys.* 6 (2008) 13–15.
- [35] I.M. Pankratov, et al., Behavior of RF discharge plasmas in the Uragan-3M and Uragan-2M torsatrons, *Contrib. Plasma Phys.* 50 (2010) 520–528, <https://doi.org/10.1002/ctpp.200900012>.
- [36] V.E. Moiseenko, et al., RF plasma production and heating below ion-cyclotron frequencies in Uragan torsatrons, *Nucl. Fusion*. 51 (2011), 083036, <https://doi.org/10.1088/0029-5515/51/8/083036>.
- [37] V.S. Voitsenya, et al., Progress in stellarator research in Kharkov IPP, *Phys. Scr.* T161 (2014), 014009, <https://doi.org/10.1088/0031-8949/2014/T161/014009>.
- [38] V.E. Moiseenko, et al., Progress in stellarator research at IPP-Kharkov, *Nukleonika* 61 (2016) 91–97, <https://doi.org/10.1515/nuka-2016-0016>.
- [39] V.E. Moiseenko, et al., Alfvén plasma heating in stellarator Uragan-2M, *Ukrainian J. Phys.* 62 (2017) 311–317, <https://doi.org/10.15407/ujpe62.04.0311>.
- [40] V.E. Moiseenko, Yu.V. Kovtun, I.E. Garkusha, Status and prospects in stellarator research at IPP KIPT, *Probl. At. Sci. Technol. Ser.: Plasma Phys.* 1 (2021) 3–8, <https://doi.org/10.46813/2021-131-003>.
- [41] C.D. Beidler, et al., Physics studies for the URAGAN-2M torsatron, in: *plasma physics and controlled nuclear fusion research 1990, in: 13th Conference Proceedings Vol. 2*, 1990, pp. 663–675, Oct.
- [42] A.A. Shishkin, Torsatron type system with the small pitch angle of helical windings and additional toroidal field coils – Uragan-2M (Principal Physics Issues), NSC KHPIT, Kharkov, 2005. Preprint KHPIT 2005-2.
- [43] G.G. Lesnyakov, et al., Studies of magnetic surfaces in the Uragan-2M Torsatron, in: *23rd European Physical Society Conference on Controlled Fusion and Plasma Physics*, Kiev Vol. 20C, 1996, pp. 547–550, 24–28 June, Part II.
- [44] G.G. Lesnyakov, A.N. Shapoval, About the values of the stray environment fields to toroidal magnetic field ratio in the Uragan-2M torsatron, *East Eur. J. Phys.* 3 (2016) 92–100.
- [45] V.V. Nemov, et al., Calculation of the magnetic surfaces of the Uragan-2M torsatron with zero current in a single toroidal magnetic field coil, *Probl. At. Sci. Technol. Ser.: Plasma Phys.* 6 (2016) 36–39.
- [46] G.P. Glazunov, et al., Thermal desorption diagnostics in the Uragan-2M stellarator, *Fusion Eng. Des.* 170 (2021), 112716, <https://doi.org/10.1016/j.fusengdes.2021.112716>.
- [47] A.V. Lozin, et al., Uragan-2m gas mixing system, *Probl. At. Sci. Technol. Ser.: Plasma Electronics and New Methods of Acceleration*. 4 (2021) 195–199, <https://doi.org/10.46813/2021-134-195>.
- [48] R.O. Pavlichenko, et al., First measurements of line electron density in Uragan-2M plasmas via 140 GHz heterodyne interferometer, *Probl. At. Sci. Technol. Ser.: Plasma Phys.* 1 (2017) 257–260.
- [49] R.O. Pavlichenko, et al., A high speed 140 GHz microwave interferometer for density fluctuation measurements in Uragan-2M stellarator, *Probl. At. Sci. Technol. Ser.: Plasma Phys.* 6 (2018) 332–335.
- [50] V.E. Moiseenko, et al., Three half-turn antennas start-up, *Probl. At. Sci. Technol. Ser.: Plasma Phys.* 1 (2019) 263–266.
- [51] A.S. Slavyj, et al., Distribution of 0.2–4.5 keV plasma ions in set of U-2M discharges, *Probl. At. Sci. Technol. Ser.: Plasma Phys.* 1 (2021) 25–30, <https://doi.org/10.46813/2021-131-025>.
- [52] S.P. Gubarev, et al., Data acquisition system for Uragan-2M, *Probl. At. Sci. Technol. Ser.: Plasma Phys.* 6 (2008) 227–229.
- [53] S.P. Gubarev, et al., The acquisition system of experimental data for Uragan-2M, *Probl. At. Sci. Technol. Ser.: Plasma Phys.* 1 (2011) 182–184.
- [54] V.N. Lyashchenko, et al., Synchronization system for experiments research installation Uragan-2M, *J. Kharkiv Natl. Univ. Phys. Ser.: Nuclei, Particles, Fields*. 880 (2009) 113–119.
- [55] V.B. Korovin, E.D. Kramskoy, Radio-frequency equipment for Uragan stellarators, *Probl. At. Sci. Technol. Ser.: Plasma Phys.* 6 (2012) 19–21.
- [56] Hayward W.H., Introduction to radio frequency design, 1st ARRL ed. Newington, 1994.
- [57] L. Lu, Modelling of plasma-antenna coupling and non-linear radio frequency wave-plasma-wall interactions in the magnetized plasma device under ion cyclotron range of frequencies, Université de Lorraine, 2016. Accelerator Physics [physics.ac-ph].
- [58] Ye.O. Kazakov, et al., Physics and applications of three-ion ICRF scenarios for fusion research, *Phys. Plasmas* 28 (2021), 020501, <https://doi.org/10.1063/5.0021818>.
- [59] J.-S. Yoon, et al., Electron-impact cross sections for deuterated hydrogen and deuterium molecules, *Rep. Prog. Phys.* 73 (2010), 116401, <https://doi.org/10.1088/0034-4885/73/11/116401>.
- [60] Yu.V. Kovtun, et al., Radio frequency wall conditioning discharges at low magnetic fields in Uragan-2M stellarator, in: *48th European Conference on Plasma Physics*, June 27 to July 1, Vol. 246A, Maastricht, 2022. ECA, O2.J503.
- [61] A.V. Lozin, et al., Cleaning of inner vacuum surfaces in the Uragan-3M facility by radio-frequency discharges, *Plasma Phys. Rep.* 39 (2013) 624–631, <https://doi.org/10.1134/S1063780X13070052>.